Regional Whole Body Fat Quantification in Mice

Xenophon Papademetris[1,2], Pavel Shkarin[2], Lawrence H. Staib[1,2],
and Kevin L. Behar[3]

[1] Departments of Biomedical Engineering,
[2] Diag. Radiology
[3] Psychiatry, Yale University New Haven, CT 06520-8042
xenophon.papademetris@yale.edu

Abstract. Obesity has risen to epidemic levels in the United States and around the world. Global indices of obesity such as the body mass index (BMI) have been known to be inaccurate predictors of risk of diabetes, and it is commonly recognized that the distribution of fat in the body is a key measure. In this work, we describe the early development of image analysis methods to quantify regional body fat distribution in groups of both male and female wildtype mice using magnetic resonance images. In particular, we present a new formulation which extends the expectation-maximization formalism commonly applied in brain segmentation to multi-exponential data and applies it to the problem of regional whole body fat quantification. Previous segmentation approaches for multispectral data typically perform the classification on fitted parameters, such as the density and the relaxation times. In contrast, our method directly computes a likelihood term from the raw data and hence explicitly accounts for errors in the fitting process, while still using the fitted parameters to model the variation in the appearance of each tissue class. Early validation results, using magnetic resonance spectroscopic imaging as a gold standard, are encouraging. We also present results demonstrating differences in fat distribution between male and female mice.

1 Introduction

Obesity is rapidly becoming an epidemic in the United States and around the world. This was particularly highlighted in a series of recent NIH workshops [5]. The relation of obesity to insulin resistance and impaired glucose tolerance leading to type 2 diabetes is well established [22, 7]. Body fat distribution in humans has also been linked to ischemic heart disease [13, 15] and cancer [2]. Further, it has been known for decades that global indices of obesity, such as the body mass index (B.M.I.), are often not an accurate predictor of the risk of diabetes and heart disease. For example, the amount of visceral abdominal fat (i.e. fat inside the abdominal cavity) seems to correlate more highly with risk for diabetes. As stated in lay language in a recent New York Times article [9], "People who are shaped like apples, carrying excess weight in the abdomen, are more likely to have diabetes and heart disease than are those built like pears,

who deposit fat in their hips, thighs and backsides." This was even further emphasized by a recent study by Klein et al [11] that demonstrated an absence of effect of liposuction on insulin resistance. This was attributed to the fact that liposuction primarily removes subcutaneous fat (i.e. fat just under the skin and outside the abdominal cavity), whose presence appears less correlated with insulin resistance.

Transgenic mouse models of obesity offer the unique ability to study the effect of factors such as age, gender, diet and therapeutic agents on disease progression, in statistically significant numbers of subjects in a tightly controlled environment. There are currently, however, no effective automated methods for the non-invasive measurement of fat distribution in rodents. While such measurements can be made invasively (via dissection [21]), non-invasive techniques will enable longitudinal studies of the same group of animals, and the development of automated image analysis techniques will facilitate large scale studies.

Multi-echo magnetic resonance imaging offers a unique non-invasive technique for quantifying soft tissue structural differences between wildtype mice and transgenic mouse models of obesity and for regional quantification of fat in a whole body image. The parameters that can be estimated from such images, namely the T1-weighted proton density and the relaxation rate r_2, offer jointly a high contrast marker for the detection of fat as well as optimal soft tissue contrast for image registration. Accurate image registration is necessary for bringing information from different mice into a common space for the purpose of statistically comparing fat distributions and morphometric differences in different groups.

In this paper, we present preliminary work aimed at the effective quantification of such images. In particular, we present a method for image classification for the purpose of determining tissue composition in terms of fat, lean muscle (non-fatty soft tissue) and bone/air. The main mathematical contribution of this work is the development of a probabilistic model for the modeling of multi-exponential data in the presence of noise for optimal tissue classification.

Our work is related to previous work in voxel based image classification and segmentation which has been extensively studied in the literature. Many of the methods in this area rely on the formalism of Markov random fields as originally presented by Geman and Geman [8]. The major application of such techniques in medical imaging has been in the voxel-based classification of brain images into gray matter, white matter and cerebro-spinal fluid. Our work is close in spirit to the approach of Wells et al. and others [24, 25], where an Expectation-Maximization strategy is used to simultaneously estimate tissue classes (gray, white, CSF) while simultaneously estimating additional parameters (in this case the bias field) which aid in the classification. Cline et al. [4] use multispectral voxel classification in conjunction with connectivity to segment the brain into tissue types. Material mixture models [12] have also been used. There has also been additional work explicitly aiming at fuzzy classification where each voxel, instead of being classified as exclusively belonging to a specific class, is given partial memberships into multiple classes e.g. [14, 19, 17]. Our proposed whole

body classification is particularly close to the work of Pham et al [17] which aims to fuzzily classify multi-spectral acquisitions using a fuzzy c-means method, and exponential fits to estimate tissue properties.

Simple thresholding techniques have been used by many investigators in more clinically focused studies to determine fat volumes (e.g. the work of Weiss et al [23].) Threshold selection, however, is often performed in an arbitrary manner and the measurements produced using such methods are highly sensitive to the exact threshold settings. There has been some work in automated fat quantification from MRI (e.g. [3, 10]) which either utilize simplified thresholding based algorithms, and/or very specific acquisition methods, which are not suitable for whole body fat quantification.

The rest of this paper reads as follows. In, Section 2, we provide details for both the conventional imaging and spectroscopic imaging (CSI) methods used to obtain both the images and the CSI data used as a gold standard. Next, in Section 3, we describe the mathematical formulation of our classification method. Validation results are presented in Section 4, and results illustrating differences in fat distribution between groups of male and female mice are presented in Section 5. Conclusions and plans for future work are discussed in Section 6.

2   Imaging and Spectroscopy Methods

Our imaging/spectroscopy methods were developed on a Bruker 4T small-animal imager with an inner diameter of 16 cm. Three-dimensional images were acquired with a resolution of approximately $0.15 \times 0.20 \times 0.15 mm$, and an imaging matrix of $128 \times 512 \times 128$, using a 3D multi-echo multi-spin (MSME) sequence with 6 echos $TE = 15, 30, 45, 60, 75, 90 ms$ and $TR = 300 ms$. This yielded six images of different contrast which in turn enable the fitting of a mono-exponential model to each voxel for the purpose of computing tissue parameters such as the relaxation rate r_2 and the T1-weighted density d. Because the dimensions of our current imaging coil were not long enough to image the full length of some male mice, in these cases mice were imaged twice with repositioning between the acquisitions and the resulting images were joined together to form the whole body image. Example images, as well as fitted mono-exponential parameters d and r_2, are shown in Figure 1.

Chemical shift spectroscopic imaging (CSI) acquisition was used as a *gold standard data* of tissue composition for a small portion of the mouse. The CSI data were acquired with a resolution of $0.4 \times 0.4 \times 1 mm^3$, dimensions $64 \times 64 \times 12$, and a spectral width of $4006 Hz$ resulting in good water and fat separation. Fat was quantified by integrating the resulting spectra for each voxel around the fat peak, as was done in the images shown in Figure 2 (on page 375). Although the acquisition time required for CSI is prohibitively long for routine work (more than two hours for a small section of the mouse), these data provide a gold standard for the validation of faster acquisitions (such as our multi-echo data) combined with more rigorous image analysis techniques.
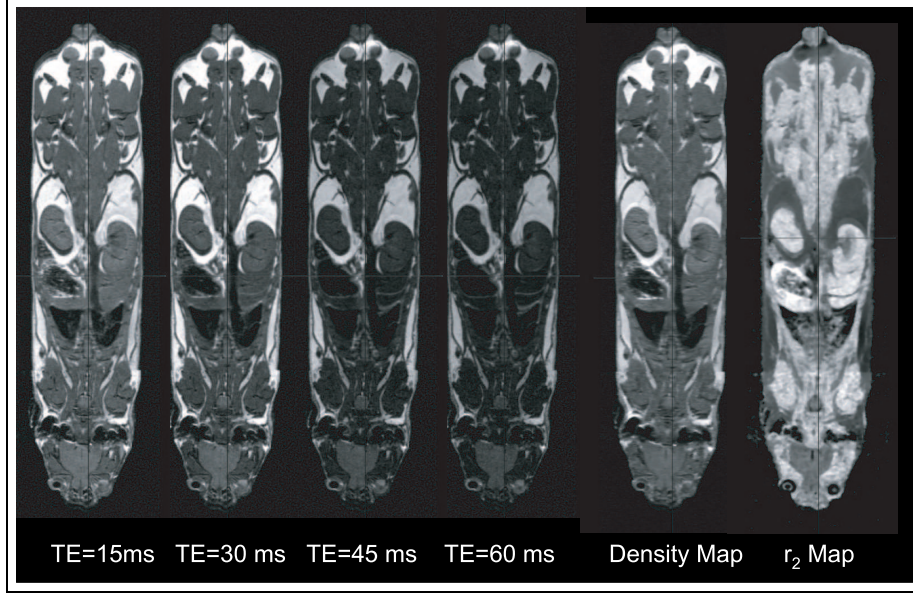
Fig. 1. Example images from multi-echo acquisitions. *Leftmost four columns:* Four different contrasts obtained using a multi-echo sequence. Rightmost two columns: Exponential fit of T1-weighted density and relaxation rate r_2

3   Tissue Classification

In this section, we describe our methodology for tissue classification from MRI. Our method for classification extends the EM-like classification methods of Wells et al and Zhang et al [24, 25], to properly apply to the vector-valued imaged data that are available to us.

Image Model: We acquire a number $N_e = 6$ of images at multiple echo times $T_e = [15, 30, 45, 60, 75, 90]$ ms, and we model the image intensity at image location $\mathbf{x}$ for a given T_e using a mono-exponential model:

$$I(\mathbf{x}, T_e) = d(\mathbf{x})e^{-T_e r_2(\mathbf{x})} + e_f(\mathbf{x}) \tag{1}$$

where T_e is the echo-time for the acquisition, $d(\mathbf{x})$ and $r_2(\mathbf{x})$ are the T1-weighted proton density and the relaxation rate at location $\mathbf{x}$ ($r_2 = 1/t_2$, where t_2 is the relaxation time), and e_f is the noise term, which we assume to be normally distributed.

For the purpose of the classification, we assume that any given voxel belongs to one of three classes $c = [\ 1{=}\text{bone/air},\ 2{=}\text{lean muscle},\ 3{=}\text{fat}\ ]$, and that the density d and relaxation rate r_2 for each class can be described as independent normally distributed random variables with means m_d, m_{r2} and standard deviations s_d, s_{r2}. We group the parameters for each class $i \in [1, 2, 3]$ into a parameter

vector $\theta_i = [m_d^i, m_{r2}^i, s_d^i, s_{r2}^i]$, and further concatenate the three parameter vectors θ_i into a global parameter vector Θ. In addition, we define the labeling function $M(\mathbf{x})$ which determines the class value for each voxel. $M(\mathbf{x})$ can take values $[1, 2, 3]$. At each image location $\mathbf{x}$ (we will drop the explicit dependence on $\mathbf{x}$ from here on), we estimate the optimal values of d and r_2. This is accomplished by minimizing a standard least squares merit function of the form:

$$\chi^2 = \sum_{j=1}^{N_e} \frac{\left(I(\mathbf{x}, T_e(j)) - de^{-T_e(j)r_2}\right)^2}{\sigma_n^2} \quad = \sum_{j=1}^{N_e} \frac{e_f(j)^2}{\sigma_n^2} \tag{2}$$

We label the optimal estimates at location $\mathbf{x}$ as $\hat{d}$ and $\hat{r}_2$, and σ_n is an estimate of the image noise at this location. We model the fitting errors $e_f(i)$ as independent and normally distributed with zero mean. The quality of the fit can be modeled using the Student's t distribution with $N_e - 2$ degrees of freedom [17]. Hence, we can compute at each voxel a probability of fit $q(\mathbf{x})$[18], given the optimal residual error χ^2. Further, we can estimate the variance of the fitting error e_f, s_e^2 which will be useful in the classification process. In summary, the application of this procedure at each voxel results in the computation of optimal tissue parameters $(\hat{d}, \hat{r}_2)$, the likelihood that the model is applicable q, and the variance of the fitting error s_e^2.

Classification Algorithm: The goal of our classification strategy can then be expressed as estimating the optimal segmentation M and parameter vector Θ given the input image vector $\mathbf{I}$. We express this mathematically as:

$$\hat{M}, \hat{\Theta} = \frac{\arg\max}{M, \Theta} \, p(M, \Theta | \mathbf{I}) \tag{3}$$

As is commonly done, this can be solved iteratively (where k labels the iteration) in the same spirit as the EM-framework as:

E-Step: $\Theta^k = \frac{\arg\max}{\Theta} p(\Theta | \mathbf{I}, M^{k-1})$, **M-Step:** $M^k = \frac{\arg\max}{M} p(M | \mathbf{I}, \Theta^k)$ (4)

where at iteration k, in the E-Step we estimate a new set of parameters Θ^k given the current classification M^{k-1} and then, in the M-Step, using the newly estimated Θ^k we estimate a new classification M^k.

E-Step: This is straightforward. For each class i we estimate the mean and standard deviation of d and r_2 by a weighted sum of the $\hat{d}$ and $\hat{r}_2$ of all the voxels where $M = i$, using the quality of fit terms q as the weights. This ensures that parameter estimates from better fits are weighted more heavily in the estimation process [17].

M-Step: This takes the form of a Bayesian a-posterior maximization. First we express

$$\hat{M} = \frac{\arg\max}{M} \log p(M | \mathbf{I}, \Theta^k) = k_1 + \log p(\mathbf{I}, \Theta^k | M) + \log p(M) \tag{5}$$

where k_1 is a constant. This equation is easily maximized by a greedy search strategy as M can only take values of $1, 2, 3$. The prior term on the classification, $p(M)$, can be defined by modeling M as a Markov random field resulting in a Gibbs distribution for M of the form: $P(M) = e^{-k_m U(M(\mathbf{x}))}$ [25], which ensures local smoothness of the classification (k_m is a normalization constant.) We express the likelihood (or data-adherence) term for each possible value of $M = i$ as:

$$p(\mathbf{I}, \Theta^k | M = i) = p(\mathbf{I} | \Theta^k, M = i) P(\Theta_k | M = i) \propto \Pi_{j=1}^{N_e} p(I(T_e^j) | \theta^i) \qquad (6)$$

The term $p(I(T_e^j) | \theta^i)$ can be derived using the imaging model (Equation 1). First we linearize this using a Taylor series expression as:

$$I(T_e^j) \approx m_d^i e^{-T_e^j m_{r2}^i} + (d - m_d^i) e^{-T_e^j m_{r2}^i} + (r_2 - m_{r2}^i) T_e^j m_d^i e^{-T_e^j m_{r2}^i} + e_f \qquad (7)$$

By assuming that d, r_2 and e_f are normally distributed random variables, we can conclude that the conditional density $p(I(T_e^j) | \theta^i)$ is also a normal distribution, as $I(T_e^j)$ is effectively a weighted sum of three normal random variables. Further we can derive the mean and standard deviation of this distribution as:

$$\text{Mean}(p(I(T_e^j) | \theta^i)) = \mu(M, T_e^j) = m_d^i e^{-T_e^j m_{r2}^i}, M = i \qquad (8)$$

$$\text{Variance}(p(I(T_e^j) | \theta^i)) = \sigma^2(M, T_e^j) = (T_e^j m_{r2}^i)^2 (s_d^2 + (m_d^i)^2 T_e^2 s_{r2}^2), M = i \; (9)$$

Based on this derivation, we can express Equation 5 in its final form as:

$$\hat{M} = \begin{array}{c} \arg\min \\ M \end{array} \underbrace{\sum_{j=1}^{N_e} \frac{\left(I(T_e^j) - \mu(M, T_e^j)\right)^2}{2\sigma(M, T_e^j)^2} - log\sigma(M, T_e^j)}_{\text{Vector Data Adherence Term}} - \underbrace{k^m U(M)}_{\text{Smoothness}} \qquad (10)$$

This formulation is superior to the more standard approach where the classification is performed directly on fitted tissue parameters (e.g. in this case the T1-weighted density d and the relaxation rate r_2) because it takes into account directly the fact that such parameter fitting is an approximation to the real data. In cases where the local parameter fit is inaccurate (i.e. the residual error in the fitting of d and r_2, which is not uncommon in motion-corrupted data) a standard classification based on these estimates can yield erroneous results, whereas by performing the classification using the original image data such errors can be avoided. Consider, for example, the case where a mono-exponential model badly approximates the data at a given voxel. If the fitted parameters are used, the data adherence term will push for the voxel to be classified in one of the given classes regardless. In our method, the values for the (vector) data adherence term will be high for all classes, hence allowing the local classification to be driven by the smoothness term as is appropriate in cases of uncertain data.

Initialization: The algorithm is initialized using a k-means clustering procedure [6, 17], which initially forms clusters based on the fitted density measurements $\hat{d}$. Then, using the output as a starting point, the algorithm performs a joint clustering on the pair $[\hat{d}, \hat{r}_2]$.

4   Validation of Segmentation Using CSI

We performed preliminary validation of the MRI-based fat quantification algorithm by comparing its output to a direct measure of fat using chemical shift spectroscopic imaging (CSI). While CSI provides high quality measurements, the imaging time is *prohibitive for in-vivo* whole body imaging. We acquired both whole body MR images and also CSI data covering a small portion of the abdomen (typically 2.5x2.5x2 cm^3) of 12 wildtype C57BL6 mice (6 male, 6 female, average age 11 weeks), using the methods described in Section 2.

CSI Processing. The CSI data were first corrected to align the water peaks in the spectra of the individual voxels (as shown in Figure 2 (top right)). Next we
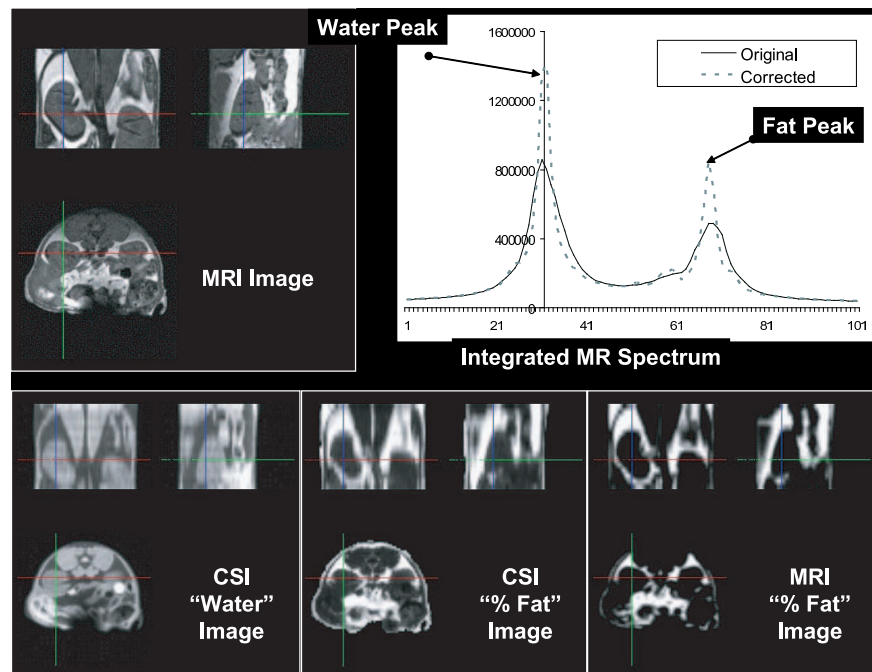

Fig. 2. Preliminary validation of the MRI-based fat measurements using spectroscopic (CSI) imaging. (Top Left) Section of the MRI image for which CSI data was acquired. (Top Right) Integrated MRS Spectrum from all CSI voxels illustrating the effect of correcting for local field inhomogeneities by shifting the individual CSI-voxel water peaks to the center of the spectrum. Note that both the water and the fat peaks become higher and narrower as a result of the correction. (Bottom Left) Spectroscopic-"water" image showing contrast that is similar to that obtained using MRI – without the fat . (Bottom Middle) Spectroscopic "% fat" image (Bottom Right) Fat probability map generated by the classification algorithm and MRI, at the same resolution as the CSI data. The correlation between the two fat maps was 0.78. When the small signal dropout region near the mouse's back is excluded the correlation rises to 0.82

Table 1. Quantitative validation of the MRI-based fat measurements with CSI. The total amount of fat in the imaged region from CSI (CSIFAT) is compared with MRI derived measurements (MRIFAT) as estimated by our algorithm (using three different smoothness parameters 0.1,0.5,1.0). The *voxelwise* correlation between the CSI percentage fat map and the algorithm output is given in the rightmost three columns. (The mouse identifier begins with 'F' for female mice and 'M' for male mice.)

Mouse	CSI FAT	MRI FAT			Correlation		
		0.1	0.5	1	0.1	0.5	1
F1	269271	279303	275568	271401	0.574	0.570	0.565
F2	295106	215768	210516	205431	0.520	0.517	0.512
F3	305127	178272	174510	170722	0.506	0.502	0.498
F4	286950	342248	338066	335099	0.542	0.537	0.530
F5	245584	170922	165038	158983	0.413	0.407	0.401
F6	363370	299371	294440	289295	0.608	0.605	0.602
M1	648171	700656	694753	686846	0.656	0.654	0.653
M2	1043136	659980	661060	659450	0.744	0.744	0.744
M3	451314	300178	296097	291818	0.744	0.743	0.742
M4	1123495	824133	820210	814955	0.779	0.778	0.777
M5	1972404	1687532	1686527	1685327	0.854	0.854	0.854
M6	512522	310780	307982	303555	0.790	0.789	0.789
Overall	7516450	5969141.1	5924766.5	5872883	**0.748**	**0.748**	**0.747**

computed a water signal and a fat signal for each voxel by integrating over the appropriate portions of the spectrum around the water and fat peaks respectively. A water image is shown in Figure 2 (bottom left), and a percentage fat image is shown in Figure 2 (bottom middle).

MRI-based Fat Quantification. Our algorithm was used to quantify fat in the MRI data and a corresponding MRI percentage fat image was computed, by first rigidly registering the MRI image to the MRS 'water image' using the method by Studholme et al. based on normalized mutual information[20] (top left, and bottom left of Figure 2 respectively) and computing the percentage of MRI voxels in the space occupied by a single CSI voxel labeled as fat by the algorithm. The results are tabulated in Table 1, and the overall trend is encouraging. The overall correlation (obtained by concatenating the fat maps from all the mice and computing a single correlation) was approximately 0.75 and the algorithm's total fat estimate was approximately 80% of the CSI total fat estimate. Further the output of the algorithm was fairly insensitive to the setting of the smoothness parameter as shown in the table.

For the male mice, the CSI slices were acquired in the kidney region where fat content is generally higher, whereas for the female mice CSI slices were through the liver where the fat is more dispersed inside the organ. The lower correlations for the female mice were expected. The error for the male mice is less as the fat around the kidney is easier to quantify from MRI (and see visually). This may be due to our hard classification strategy which does not allow for partial voxel labeling. Also, in general our approach under-estimated the total amount of fat possibly due to the inability of the mono-exponential model to accurately quantify fat dispersed in tissue.

5   Quantification of Group Differences

5.1   Fat Quantification in Male and Female Mice via ROI Analysis

To illustrate the potential applications of our methodology in the evaluation
of groups of mice, we performed regional fat quantification for two groups of
mice, a group of $N = 5$ male mice and a group of $N = 5$ female mice. The two
groups were approximately age matched (average age 10.6 vs 10 weeks). They
are a subset of the mice used for evaluation of our tissue classification algorithm
presented in Section 4, in particular two mice were omitted from the original
$N = 12$ mice of Table 1 for the purpose of this analysis to make the groups
approximately age matched.

Our tissue classification strategy described in Section 3 was used to classify
the images. Using this classification, we computed the following measures which
are tabulated in Table 2: (a) Total mouse volume, (b) Total body fat volume,
(c) Abdominal fat volume – this was defined as the total volume of fat inside the
abdomen. A region of interest (ROI) inside the abdomen was defined by the semi-
automatically extracted abdominal surfaces in each mouse. (d) Subcutaneous
Fat Volume – defined as the total amount of fat outside the abdomen, (e) %
abdominal fat, defined as the ratio of abdominal fat to total fat and (f) % body
fat, defined as the ratio of total fat volume to total mouse volume.

The results tabulated in Table 2, demonstrate that in these two (admittedly
small) groups, male mice tend to be bigger and have proportionally more fat than
female mice, Further, we illustrate our ability to quantify regional fat measures
such as abdominal fat, as opposed to simply whole body fat. We additionally note
that the computed % body fat numbers are in the same range as those reported
in the literature[1] using a whole body MR-spectrometer on similar mice.

Table 2. Quantification of key parameters using our tissue classification algorithm
(*Top:* M = Males $N = 5$. *Bottom:* F = Females $N = 5$). Mice were approximately
age-matched (10.6 vs 10 weeks old)

	M1	M2	M3	M4	M5	Average
Age (weeks)	9	10	10	12	12	*10.6*
Volume (mm³)	15265	20267	15467	21497	21433	*18785.8*
Total Fat (mm³)	2219	3272	2338	5371	6223	*3884.6*
Abd. Fat (mm³)	1002	1678	1090	2489	2731	*1798.0*
Sub. Fat (mm³)	1217	1594	1248	2882	3492	*2086.6*
% Abd Fat	45%	51%	47%	46%	44%	*47%*
% Body Fat	15%	16%	15%	25%	29%	*20%*

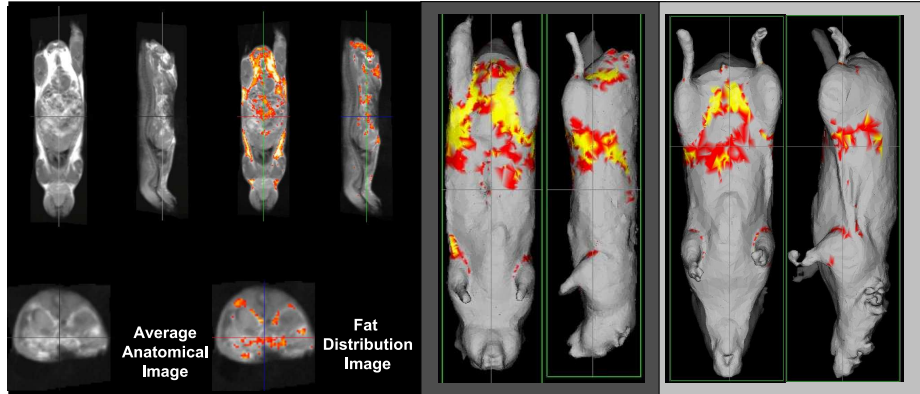|	F1	F2	F3	F4	F5	Average
Age (weeks)	8	8	11	11	12	*10.0*
Volume (mm³)	11070	11780	14507	13583	14530	*13094.0*
Total Fat (mm³)	1787	1519	2247	1823	2097	*1894.6*
Abd. Fat (mm³)	640	743	1001	805	864	*810.6*
Sub. Fat (mm³)	1147	776	1246	1018	1233	*1084.0*
% Abd. Fat	36%	49%	45%	44%	41%	*43%*
% Body Fat	16%	13%	15%	13%	14%	*14%*

Fig. 3. Left: Average anatomical image (left) and fat distribution image (right) from $N = 5$ male mice, computed using non-rigid registration. The fat distribution is overlaid on the average anatomical image (right) where the color scale is such that voxels shown in red were classified as fat in at least half the mice, with progressively brighter shades of yellow indicating that those areas were classified as fat in more mice. **Middle & Right:** Fat distributions of $N = 5$ male (middle) and $N = 5$ female (right) projected onto the outer skin surface of the reference male and female mice respectively. At each point in the surface we plot the average value of the fat distribution on a line segment of length 7 mm parallel to the local surface normal

5.2   Fat Distributions in Male and Female Mice

For the same $N = 5$ male and $N = 5$ female mice used in the previous section we computed fat distribution maps by (a) registering the individual male and female mice into a common space using our integrated registration method [16] – that used both image
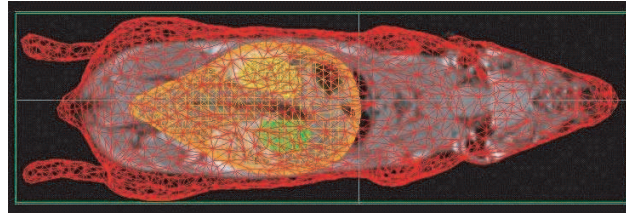

Fig. 4. Example of a point-set used for registration – from a female mouse. Red: outer skin surface, orange: abdominal surface, green and yellow: right and left kidney surfaces respectively

intensities and points sampled from pre-segmented surfaces (an example is shown in Figure 4), and (b) averaging the warped individual fat maps to generate average fat distribution maps for each group. The fat distribution maps are shown in Figure 3. Visually it is again obvious that in this case the male mice had substantially more fat, especially in the area around the reproductive organs (between the rear two legs). Such fat distributions generated by the registration of individual mouse tissue classification maps to a common space afford a direct look of what the typical fat distribution is in a group of mice.

6   Conclusions and Future Work

With the segmentation and quantification method described in this paper it has been possible to estimate regional body fat which overcomes a number of inadequacies in previous studies. The current method achieves an accurate quantification of subcutaneous fat pads, however the accuracy of the method to detect intra-organ fat (e.g. in the liver) which is dispersed in normal tissue is limited by its reliance on binary classification and mono-exponential tissue modeling. To address these limitations, it should be possible to use a larger number of non-uniformly spaced echos to enable the robust estimation of multi-exponential tissue models, which in turn will enable the use of fuzzy classification techniques. Additional ongoing work aims to optimize whole body mouse non-rigid registration to address the issue of forming composite fat maps and eliminating the need for the manual ROI analysis, which was used in the results presented in Section 5.1. The classification methods presented in this paper are also applicable in both human and rodent neuroimaging in cases where multi-echo data is available.

References

1. DE Berryman, EO List, KT Coschigano, K Behar, JK Kim, and JJ Kopchick. Comparing adiposity profiles in three mouse models with altered GH signaling. *Growth Hormone & IGF Research*, 14:309–18, Aug 2004.

2. E. E. Calle and R. Kaak. Overweight, obesity and cancer: Epidemiological evidence and proposed mechanisms. *Nature Reviews Cancer*, 4:579–591, 2004.

3. K. K. Changani, A. Nicholson, A. White, J.K. Latcham, D.G. Reid, and J. C. Clapham. A longitudinal magnetic resonance imaging (MRI) study of differences in abdominal fat distribution between normal mice and lean overexpressors of mitochondrial uncoupling protein-3 (UPC-3). *Diabetes, Obesity and Metabolism*, 5:99–105, 2003.

4. H. E. Cline, W. E. Lorensen, R. Kikinis, and F. Jolesz. Three-dimensional segmentation of MR images of the head using probability and connectivity. *Journal of Computer Assisted Tomography*, 14(6):1037–1045, Nov. /Dec. 1990.

5. NIH Obesity-Related Scientific Meetings Conferences and Workshops. http://obesityresearch.nih.gov/news/meetings-archive.htm.

6. R. Duda and P. Hart. *Pattern Classification and Scene Analysis*. John Wiley and Sons, N.Y., 1973.

7. DJ Evans, RG Hoffmann, RK Kalkhoff, and AH Kissebah. Relationship of body fat topography to insulin sensitivity and metabolic profiles in premenopausal women. *Metabolism*, 33(1):68–75, Jan 1984.

8. D. Geman and S. Geman. Stochastic relaxation, Gibbs distribution and the Bayesian restoration of images. *IEEE Trans. Pattern Analysis and Machine Intelligence*, 6(6):721–741, November 1984.

9. Denise Grady. The secret life of a potent cell. *The New York Times*, F::1, July, 6th 2003.

10. S. A. Gronemeyer, R. G. Steen, W. M. Kauffman, W. E. Reddick, and J. O Glass. Fast adipose tissue (FAT) assesment by MRI. *Magnetic Resonance Imaging*, 18:815–818, 2000.

11. S Klein, L. Fontana, V. Young, Leroy. C., R. Andrew, C. Kilo, B. W. Patterson, and B. S. Mohammed. Absence of an effect of liposuction on insulin action and risk factors for coronary heart disease. *New England Journal of Medicine*, 350(25):2549–2557, June, 17th 2004.

12. Z. Liang, R. F. Jaszczak, and R. E. Coleman. Parameter estimation of finite mixtures using the EM algorithm and information criteria with application to medical image processing. *IEEE Trans. Nucl. Sci.*, 39(4):1126–1133, 1992.

13. JE Manson, GA Colditz, MJ Stampfer, WC Willett, B Rosner, RR Monson, FE Speizer, and CH Hennekens. A prospective study of obesity and risk of coronary heart disease in women. *N Engl J Med.*, 322(13):882–9, Mar 1990.

14. A. Noe and J. C. Gee. Partial volume segmentation of cerebral MRI scans with mixture model clustering. In *Information Processing in Medical Imaging (IPMI)*, pages 423–430, 2001.

15. LO Ohlson, B Larsson, K Svardsudd, L Welin, H Eriksson, L Wilhelmsen, P Bjorntorp, and G. Tibblin. The influence of body fat distribution on the incidence of diabetes mellitus. 13.5 years of follow-up of the participants in the study of men born in 1913. *Diabetes*, 34(10):1055–8, Oct 1985.

16. X. Papademetris, A. Jackowski, R. T. Schultz, L. H. Staib, and J. S. Duncan. Integrated intensity and point-feature nonrigid registration. In *Medical Image Computing and Computer Aided Intervention (MICCAI)*, 2004.

17. D. L. Pham and J. L. Prince. Adaptive fuzzy segmentation of magnetic resonance images. *IEEE Transactions on Medical Imaging*, 18(9):737–752, September 1999.

18. W. H. Press, S. A. Teukolsky, W. T. Vetterling, and B. P. Flannery. *Numerical Recipes in C: The Art of Scientific Computing*. Cambridge University Press, Cambridge, U. K., 1994, Second Edition.

19. D.W. Shattuck, S. R. Sandor-Leahy, K.A. Schaper, D.A. Rottenberg, and R.M. Leahy. Magnetic resonance image tissue classification using a partial volume model. *NeuroImage*, 13(5):856–876, May 2001.

20. C. Studholme, D. Hill, and D. Hawkes. Automated three-dimensional registration of magnetic resonance and positron emission tomography brain images by multiresolution optimisation of voxel similarity measures. *Medical Physics*, 24(1):25–35, 1997.

21. Y-S. Tsai, H-J Kim, N. Takahashi, H-S. Kim, J. Hagaman, J. K. Kim, and N. Maeda. Hypertension and abnormal fat distribution but not insulin resistance in mice with p465l pparγ. *J. Clin. Invest.*, 114:240–249, 2004.

22. R. Weiss, S. Dufour, S. Taksali, W. V. Tambolrane, K. F. Petersen, R. C. Bonadonna, L. Boselli, G. Barbetta, K Allen, F. Rife, M. Savoye, J. Dziura, R. Sherwin, G. I. Shulman, and S. Caprio. Prediabetes in obese youth: a syndrome of impaired glucose tolerance, severe insulin resistance and altered myocellular and abdominal fat partitioning. *Lancet*, 362:951–7, 2003.

23. R. Weiss, S.E. Taksali, S. Dufour, C.W. Yeckel, X. Papademetris, G. Kline, W.V. Tamborlane, J. Dziura, G.I. Shulman, and S. Caprio. The "Obese Insulin Sensitive adolescent" – importance of adiponectin and lipid partitioning. *J. Clin Endocrinol. Metab.*, March 2005.

24. W.M. Wells, R. Kikinis, W.E.L Grimson, and F. Jolesz. Adaptive segmentation of MRI data. *IEEE Transactions on Medical Imaging*, 15:429–442, 1996.

25. Y. Zhang, M. Brady, and S. Smith. Segmentation of brain MR images through a hidden markov random field model and the expectation maximization algorithm. *IEEE Transactions on Medical Imaging*, 20(1):45–57, 2001.